COMMUNICATIONS IN NUMERICAL METHODS IN ENGINEERING
Commun. Numer. Meth. Engng 2000; **00**:1–6 *Prepared using* cnmauth.cls *[Version: 2002/09/18 v1.02]*

Quality meshing based on STL triangulations for biomedical simulations

E. Marchandise [1] *, G. Compère[1] , M. Willemet[1] , G. Bricteux[1] , C. Geuzaine[2], and J-F Remacle[1]

[1] *Université catholique de Louvain, Institute of Mechanics, Materials and Civil Engineering (iMMC), Avenue G.Lemaitre, 4 1348 Louvain-la-Neuve, Belgium*
[2] *Université de Liège, Department of Electrical Engineering and Computer Science, Montefiore Institute B28, 4000 Liège, Belgium*

SUMMARY

This work describes an automatic approach to recover a high quality surface mesh from low-quality or oversampled inputs (STL-files) obtained from medical imaging through classical segmentation techniques. The approach combines a robust method of parametrization based on harmonic maps [1] with a recursive call to a multi-level edge partitioning software. By doing so, we are able to get rid of the topological and geometrical limitations of harmonic maps. The overall remeshing procedure is implemented, together with the finite element discretization procedure required for computing harmonic maps, in the open-source mesh generator Gmsh [2]. We show that the proposed method produces high quality meshes and we highlight the benefits of using those high quality meshes for biomedical simulations. Copyright © 2000 John Wiley & Sons, Ltd.

KEY WORDS: surface mapping; surface meshing; parametrization; open source; remeshing; STL files; biomedical

1. INTRODUCTION

In the biomedical field geometrical data is acquired through medical imaging techniques such as CT scan or MRI. The data is then usually given to end-users as a STL triangulation that comes as the output of a surface reconstruction algorithm applied to the point cloud obtained from the medical images [3]. Those generated STL triangulations can serve as input for most volume meshing algorithms [4, 5]. Yet, those STL triangulations are generally oversampled and of very low quality, with poorly shaped and distorted triangles. This is still to date a major bottleneck in the domain of biomedical computations since the quality of the mesh impacts both on the efficiency and the accuracy of numerical solutions [6, 7]. For example, it is well known that for finite element computations, the discretization error in the finite element solution increases when the element angles become too large [8], and the condition

*Correspondence to: emilie.marchandise@uclouvain.be

number of the element matrix increases with small angles [9]. It is then desirable to modify the initial surface mesh to generate a new surface mesh with nearly equilateral triangles or with a smooth gradation of triangle density based on the geometry curvature. This procedure is called *remeshing*.

There exist mainly two approaches for surface remeshing: mesh adaptation strategies [10, 11, 12] and parametrization techniques [13, 14, 15, 16, 17, 18]. The mesh adaptation strategies belong to the direct meshing methods and use local mesh modifications in order both to improve the quality of the input surface mesh and to adapt the mesh to a given mesh size criterion. The parametrization techniques belong to the indirect meshing approach. The initial 3D surface mesh is first parametrized onto a 2D planar surface mesh; the initial surface can then be remeshed using any 2D mesh generation procedure by subsequently mapping the new mesh back to the original surface.

When a parametrization of the surface is available, it is usually better to use it for remeshing. Indeed, when a parametrization is available, ensuring that the surface mesh has the right topology is trivial. Also, as the medical geometries are often highly oversampled and of very poor quality, the numerous sampling operations are much more efficient in the parameter plane than in 3D space.

In a recent paper [1] we have introduced an efficient approach for high quality remeshing of surfaces based on a parametrization technique. The approach uses a discrete finite element harmonic map to parametrize the input triangulation onto a unit disk. By combining it with a local cavity check algorithm that enforces the discrete harmonic map to be one-to-one, we came out with a robust method for remeshing that is advantegeous compared with mesh adaptation methods. However, as it was highlighted in [1], there are two important limitations of harmonic maps, namely limitations on the genus and the geometrical aspect of the surface. Indeed, to be able to parametrize the triangulation onto a unit disk, the triangulation should be homeomorphic to a disk, i.e have a genus zero with at least one boundary. Besides, as the solution of harmonic maps tends exponentially to a constant, the triangulation should have a uniform geometrical aspect ratio to prevent non distinguishable coordinates.

In this paper, we present a robust and automatic way to overcome the topological and geometrical limitations of harmonic maps. The presented algorithm combines a discrete harmonic mapping with a multi-level edge partitioning software that recursively partitions the triangulation into a small number of charts that satisfy the topological and geometrical constraints. We show that our method renders high quality meshes and highlight the benefits of using those high quality meshes for cardiovascular and bone biomechanical simulations.

2. MESHING WITH HARMONIC MAPS

The key feature of our remeshing algorithm presented in [1] is to define a map that transforms continuously a surface $\mathcal{S} \in \mathcal{R}^3$ into a unit disk $\mathcal{S}'$ embedded in $\mathcal{R}^2$ [19, 20]. The parametrization should be a bijective function $\mathbf{u}(\mathbf{x})$:

$$\mathbf{x} \in \mathcal{S} \subset \mathcal{R}^3 \mapsto \mathbf{u}(\mathbf{x}) \in \mathcal{S}' \subset \mathcal{R}^2. \quad (1)$$

Such a parametrization exists if the two surfaces $\mathcal{S}$ and $\mathcal{S}'$ have the same topology, i.e are both zero genus surfaces ($G = 0$) and have at least one boundary ($N_B \geq 1$)†. When the surface $\mathcal{S}$ is a triangular mesh as in the case of an STL file, the genus can be easily computed from the Euler-Poincare formula:

$$G = \frac{-N_V + N_E - N_T + 2 - N_B}{2}. \tag{2}$$

where N_V, N_E, and N_T are respectively the number of vertices, edges and triangles.

Harmonic maps have been chosen for the parametrization [21, 22], by solving one Laplace problem for each coordinate:

$$\nabla^2 u = 0, \quad \nabla^2 v = 0, \tag{3}$$

with appropriate Dirichlet boundary condition for one of the boundaries $\partial\mathcal{S}_1$ of the surface $\mathcal{S}$,

$$u(l) = \cos(2\pi l/L) \quad , \quad v(l) = \sin(2\pi l/L), \tag{4}$$

and with Neumann boundary conditions for the other boundaries. In (4), l denotes the curvilinear abscissa of a point along the boundary $\partial\mathcal{S}_1$ of total length L.

The discrete harmonic map is obtained through a finite element formulation of the Laplace problem (3)–(4) on the STL triangulation. The finite element solutions provide to each internal vertex of the original triangulation $\mathbf{x}$ its local coordinates u and v. However, as shown in [1] the solution of the mapping becomes exponentially small‡ for vertices located away from $\partial\mathcal{S}_1$. As a consequence, local coordinates u and v of those far away vertices might numerically become indistinguishable (see the zoom in Fig.1). To prevent this, the geometrical aspect ratio of the surface:

$$\eta = \frac{H}{D} \tag{5}$$

should be smaller than 4. Indeed we can show that $\eta = 4$ corresponds to an area of mapped triangles of about $r_i^2 = 10^{-10}$ (see Eq. 23 and Fig. 10c in [1]). In (5), H is the maximal distance (computed on the 3D surface $\mathcal{S}$) of a mesh vertex to the boundary $\partial\mathcal{S}_1$ and D is the equivalent diameter of the boundary $\partial\mathcal{S}_1$.

Figure 1 shows both an initial triangular mesh of $\mathcal{S}$ and its map onto the unit disk. The surface $\mathcal{S}$ results from the segmentation of an anastomosis site in the lower limbs, more precisely a bypass of an occluded femoral artery realized with the patient's saphenous vein. The unit disk D contains two holes that correspond to the boundary of the femoral artery $\partial\mathcal{S}_2$ and the saphenous vein $\partial\mathcal{S}_3$ on which we have imposed Neumann boundary conditions.

Once the parametrization is computed, we use standard 2D anisotropic mesh generation procedures onto the unit disk, with the aim of producing a mesh in the real 3D space that has controlled element sizes and shapes. In order to control the surface element sizes, we define an isotropic mesh size field [2] $\delta(\mathbf{x})$ that is a function that gives the optimal mesh edge length at point $\mathbf{x}$. In the examples that will be presented, the mesh size field is chosen to be either a constant or varies according to the curvature of the geometry.

†For example, a sphere has $G = 0$ and $N_B = 0$ and a torus has $G = 1$ and $N_B = 0$.

‡In principle, the solution becomes constant far from the boundary, this constant being the average of the solution on the boundary. Yet, the average of the solution on the boundary being zero, the solution goes to zero far from the boundary.

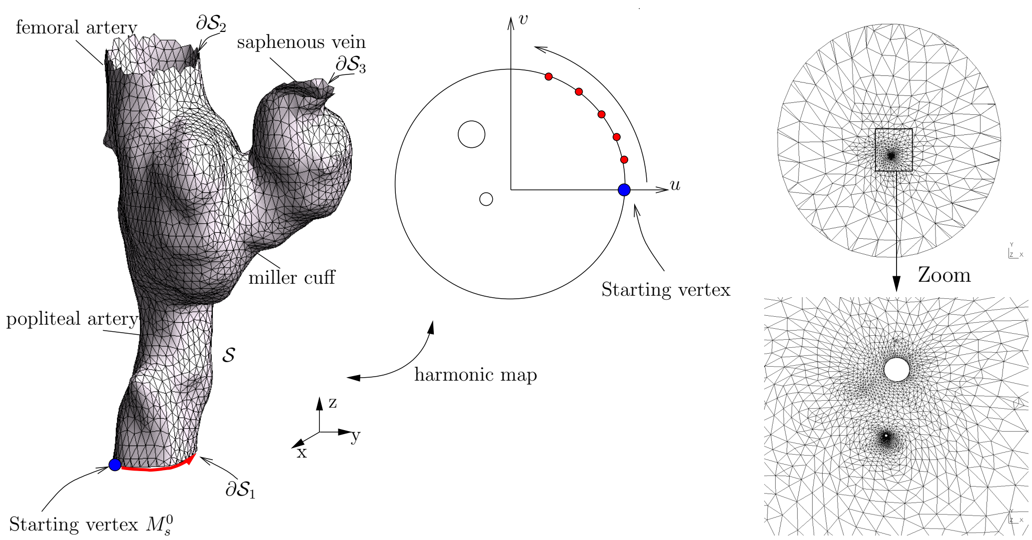

Figure 1. STL triangulation of an arterial anastomosis ($G = 0$, $N_B = 3$, $\eta = 5$) and its map onto the unit circle (left) and mapped mesh on the unit circle (right). As the geometrical ratio of the initial STL triangulation is higher than 4, the mapped triangles become very small (see zoom) in the parametric unit disk.

3. AUTOMATIC QUALITY REMESHING

In the previous section we put to the fore the topological and geometrical limitations of harmonic maps. To sum up, for the proposed discrete harmonic maps we need:

i) $G = 0$;

ii) $N_B \geq 1$;

iii) $\eta < 4$.

The first condition can be verified using Eq. (2); the second condition can be checked by looking simply at the topology of the mesh. The third condition is less trivial to assess.

In the computer graphics community, people overcome all three conditions simultaneously by using a partition scheme based on the concept of Voronoi diagrams [22] or inspired by Morse theory [18, 23]. The resulting mesh partitions are area-balanced patches that satisfy the three conditions. However, this approach results in a large number of patches and hence a large number of interfaces between those patches, which is not desirable.

We propose in this paper a fast and automatic way to overcome both topological and geometrical limitations of harmonic maps. The idea is to combine an harmonic map with a multilevel edge partitioning softwares such as Chaco [24] or Metis [25] to partition recursively the triangulation into a minimal number of partitions that satisfy the topological and geometrical conditions. Multilevel methods are attractive since they reduce the costs of spectral partitioning methods while still generating high quality partitions. These work on the connectivity graph of the mesh, but instead of trying to split this directly, the graph is first condensed through a number of levels. The condensation is achieved through clustering together vertices that are close together' to produce a graph with fewer vertices. New edges between the clusters are weighted to reflect the number of edges that existed in the larger graph. By using several levels of condensation a much smaller graph can be obtained that is easily partitioned by a method such as spectral bisection. This partitioning information can then be transfered up through the levels to the original graph.

The automatic procedure for a uniform remeshing a triangulation $\mathcal{S}$ with prescribed mesh size δ is illustrated in Figures 2 and 3 and reads as follows:

1. Check conditions (i)-(iii). If those conditions are not satisfied, recursively split the mesh with the multi-level partitioning software until satisfied. The geometrical aspect ratio η is computed approximately by using the ratio between the maximal size of the bounding box of the mesh partition and the maximal size of the bounding box of the boundaries $\partial\mathcal{S}$ of the mesh partition [26] (see illustration in Fig. 3(1)) ;

2. Remesh the lines that are the boundaries of the triangulation and the interfaces between the mesh partitions (see the interfaces between colored patches in 2a) that are represented by highlighted white lines in Fig.2b); Those lines are defined as model edges and divided into N parts as follows: $N = \int_0^L ||\mathbf{x}_{,t}|| \,/\delta dt$. The remeshed lines are embedded in the final mesh shown in Fig. 2c).

3. Compute the harmonic mapping for every mesh partition as explained in the previous section. If the boundary is composed of several parts $\partial\mathcal{S}_i$, assign the Dirichlet boundary conditions (4) to the closed boundary that has the largest bounding box.

4. Use standard surface meshers to remesh every partition in the parametric space and map the triangulation back to the original surface.

5. If a volume mesh is needed, generate a volume mesh from the new surface mesh using standard volume meshing techniques.

In our algorithm, the bounding boxes are oriented bounding boxes that are computed with the fast Oriented bounding box HYBBRID optimization algorithm presented in [26] which combines the genetic and Nelder-Mead algorithms [27].

The automatic procedure is implemented within the open source mesh generator Gmsh [2]. We show a simple example of how to use it. We suppose that we have an initial surface mesh and write the following geometry file "remesh.geo":

```
//Merge the STL triangulation
Merge "skull.stl";

// Remesh the edges (if any), and faces with the presented algorithm
Compound Surface(100) = {1};

// Create a volume and mesh given the new surface mesh
Surface Loop(2) = {100};
Volume(3) = {2};
```

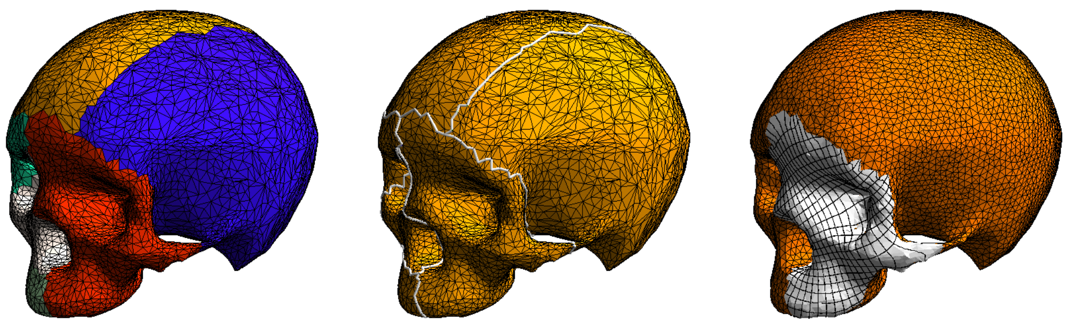

a) b) c)

Figure 2. Remeshing algorithm. a) Initial triangulation ($G = 2, N_B = 0$) that is cut into different mesh partitions of zero genus, b) Remesh the lines at the interfaces between partition, c) Compute harmonic map for every partition and remesh the partition in the parametric space ($\mathbf{u}(\mathbf{x})$ coordinates visible for one partition).

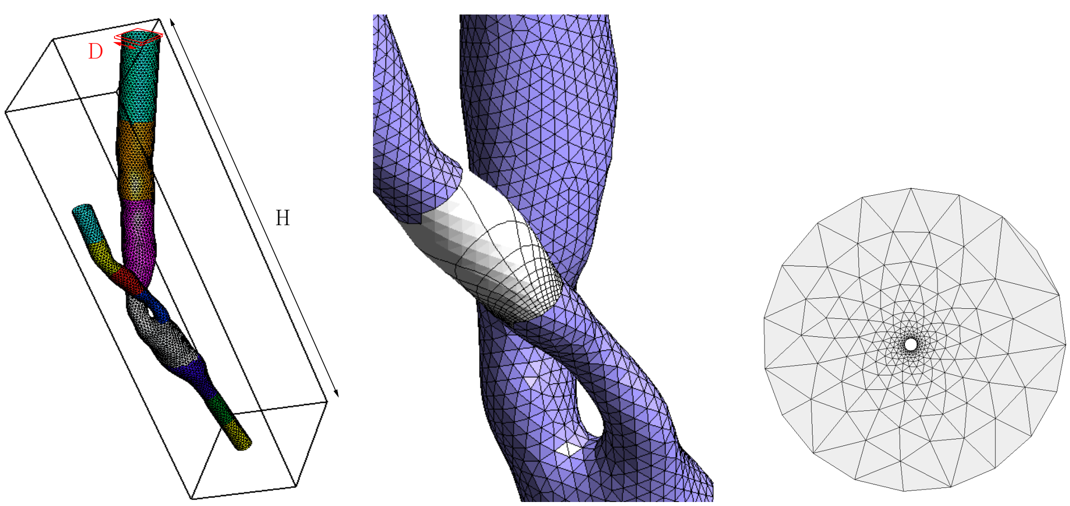

a) b) c)

Figure 3. Remeshing algorithm. a) Initial triangulation ($G = 0, N_B = 3, \eta = H/D = 16$) that is cut into different mesh partitions of uniform geometrical aspect ratio, b) The harmonic map is computed for every partition ($\mathbf{u}(\mathbf{x})$ coordinates visible for one partition) c) Remesh every partition in the parametric space. The mapped initial triangulation is shown for the partition visible on the middle image.

Other examples can be found on the Gmsh wiki: `https://geuz.org/trac/gmsh` (username: gmsh, password: gmsh) .

4. RESULTS

4.1. High quality surface and volume meshes

We have run our computational algorithm on a variety of medical geometries of arbitrary genus and complexity. Fig. 4 illustrates a uniform remeshing of respectively a skull, an upper jaw and a hemipelvis. The top figure shows the remeshing of a human skull, the middle figures the remeshing of an upper jaw that is oversampled (116k vertices) and the lower figures the remeshing of an initial poor quality mesh of an hemi-pelvis. None of those initial triangulations satisfy the topological conditions: the skull has genus $G = 2$, the jaw has genus $G = 0$ but has $N_B = 0$ and the pelvis has $G = 1$ and $N_B = 0$.

The quality of an isotropic mesh is evaluated by computing the aspect ratio of every mesh triangle as follows [2]:

$$\kappa = \alpha \frac{\text{inscribed radius}}{\text{circumscribed radius}} = 4 \frac{\sin \hat{a} \sin \hat{b} \sin \hat{c}}{\sin \hat{a} + \sin \hat{b} + \sin \hat{c}}, \tag{6}$$

$\hat{a}, \hat{b}, \hat{c}$ being the three inner angles of the triangle. With this definition, the equilateral triangle has $\kappa = 1$ and degenerated (zero surface) triangles have $\kappa = 0$.

Fig. 5 shows the quality histogram for the initial triangulation of a foot and the remeshed geometry. As seen in fig.5, the mean $\bar{\kappa}$ and minimum quality κ_{min} of the new mesh are both very high: $\bar{\kappa} = 0.94, \kappa_{min} = 0.62$. This mean quality measure was found to be constant ($\pm 2\%$) for all examples and hence independent of the initial triangulation and the mesh density. Volume tetrahedral meshes can then be created from those surface meshes. In order to measure the quality of the tetrahedral elements, we define another quality measure γ based also on the element radii ratio [2, 28]:

$$\gamma = \frac{6\sqrt{6}\, V}{S_F\, L_E},$$

V being the volume of the tetrahedron, S_F being the sum of the areas of the 4 faces of the tetrahedron, and L_E being the sum of the lengths of the 6 edges of the tetrahedron. This γ quality measure lies in the interval $[0, 1]$, an element with $\gamma = 0$ being a sliver (zero volume). When creating volume meshes from surfaces that have been remeshed with our algorithm, we obtain also quite constant γ qualities, i.e $\gamma_{min} = 0.25 \pm 10\%$ and $\bar{\gamma} = 0.7 \pm 10\%$. This is much better than the gamma quality of volumes meshes created from STL triangulations. Indeed the quality of those volume meshes is often very poor, with elements being small slivers $\gamma_{min} < 1.e^{-5}$ that will hinder or event prevent the convergence of the numerical method.

The time necessary to generate with our algorithm a new surface mesh less is less than 100 s for 10^6 elements.

4.2. Quality meshing for biomedical simulations

The two first biomedical simulations concern blood flow simulations. In the first example, blood flow in a distal anastomosis of a bypass is considered. While this problem has often been studied in-vitro in simplified geometries [**?**, **?**, **?**], the simulation of blood flow in in-vivo complex geometries is of great interest when one wants to focus on the patient-specific aspect [**?**]. As this is not the goal of this study, we refer the reader to the cited references for detailed hemodynamical analysis. We intend to illustrate in the following test case that in

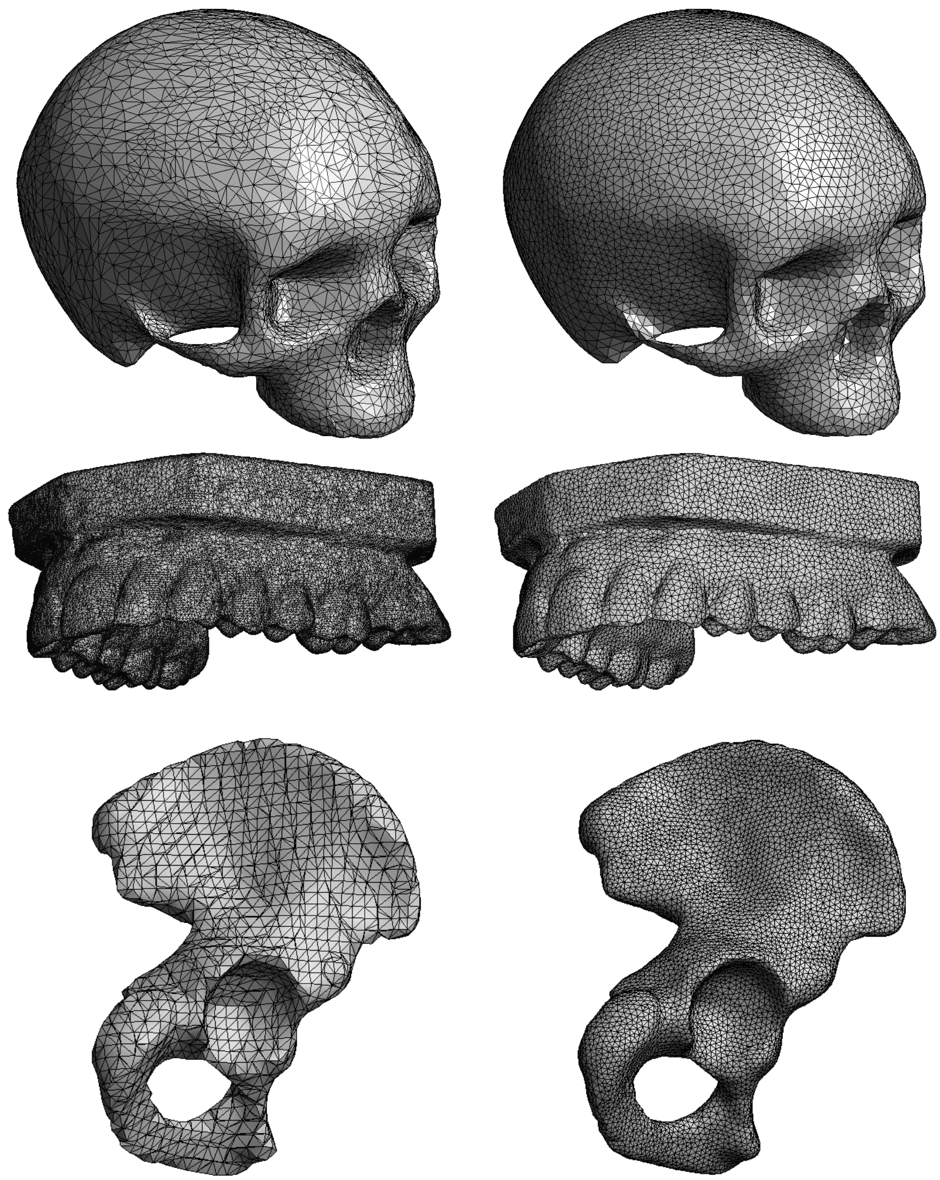

Figure 4. STL triangulations obtained from medical images (Left) that have been automatically remeshed with our automatic remeshing algorithm (Right).

real and complex geometries, a high-quality mesh is required in order to ensure the numerical convergence of the simulation. Identical conclusions have been reached in computational studies related to other biomedical applications and considering the effects of various meshing style: Vinchurkar et al [**?**, **?**] have shown the performances of different types and qualities of meshes in

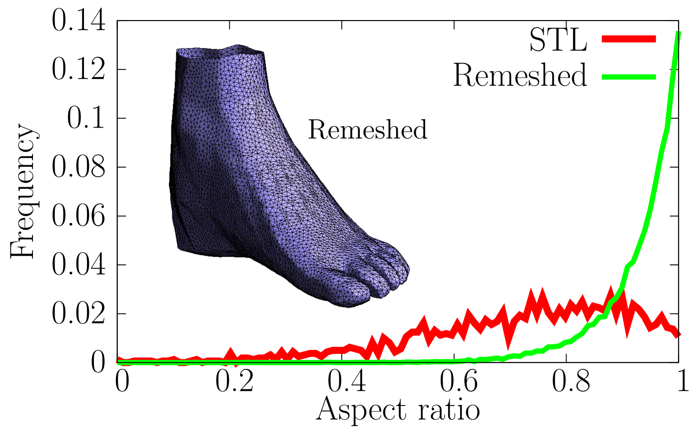

Figure 5. Plot of the quality histogram of both the STL triangulation and the remeshed surface of a scanned foot.

the complex branching geometries of the respiratory system; Liu et al [?] compared simulations in the total cavopulmonary connection using structured and unstructured meshes; Ethier and Prakash [?] studied a mesh convergence study of blood flow in a coronary artery model.

In the two following test cases, blood flow is governed by the incompressible Navier-Stokes equations for a Newtonian fluid. We use an implicit pressure stabilized finite element method that has been shown to be robust, accurate and stable [29]. The linearized system is solved by using a GMRES solver with a relative convergence tolerance of 10^{-12}. The fluid properties of blood are taken to be $\rho = 1060\, kg/m^3$ for the density and $\mu = 3.5\, Pa.s$ for the dynamic viscosity.

The first test case studies steady blood flow at Reynolds $Re = 900$ (based on the inlet diameter and average inlet velocity) in a veinous anastomosis of an occluded femoral artery (Figure 6) [30]. The anastomosis is segmented out of raw image data from a patient that underwent lower-limb bypass surgery. Two surface meshes are produced, one from the initial STL triangulation and one using the remeshing procedure based on harmonic maps. Those surface meshes then serve as input for the generation of two volume meshes of about 10^4 tetrahedra (an STL based and a remeshed based volume mesh). Table I shows the quality of these two surface and volume meshes: the remeshed mesh presents higher minimal and mean qualities that enables the flow solver to converge better (see Fig. 6).

Mesh	Surface quality		Volume quality	
	κ_{min}	$\overline{\kappa}$	γ_{min}	$\overline{\gamma}$
STL	0.0033	0.821	0.0019	0.563
Remeshed	0.6400	0.949	0.2550	0.677

Table I. Quality of the surface and volume meshes.

The simulation is run with a constant flow rate at the inlet ($\overline{Q} = 75$ ml/min), a no-slip boundary condition at the walls and a constant pressure boundary condition on the outlet surface ($p = 50\ mmHg$). Figure 6 shows the convergence rates for each of the two volume meshes. Figure 6 shows that the element quality has a significant impact on the convergence rate of the solution procedure. Indeed, the simulation on the mesh obtained from the STL converges at $1.e^{-7}$, while the remeshed mesh gives results that are two times more accurate.

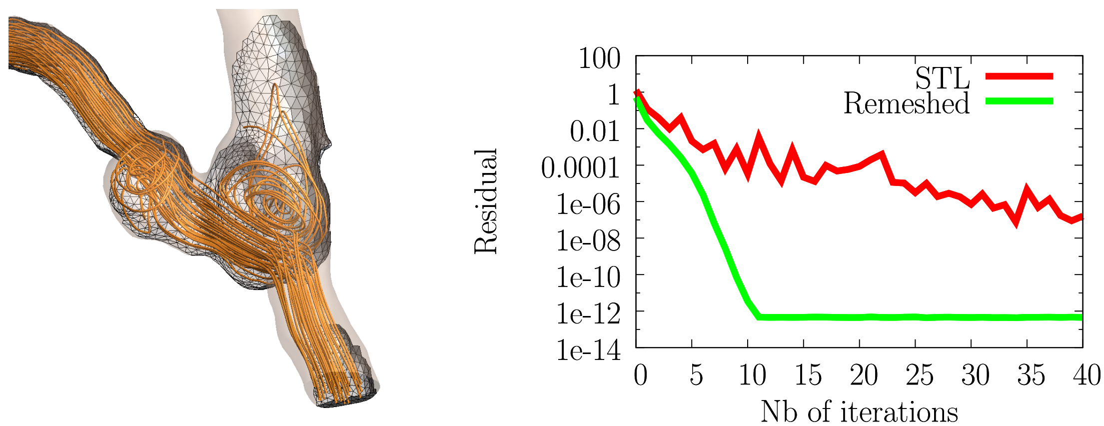

Figure 6. Blood flow simulation in an arterial bypass. The left figure shows the streamlines (zoom near the anastomosis) and the right figure shows the residual decrease for the two different volume meshes.

The next example studies the flow in a simplified aortic arch. The STL triangulation was found on the INRIA web site§. Accurate and converged numerical simulations are mandatory since it has been shown that the flow patterns and the locations of low wall shear stress (WSS) correspond with locations of aneurysm formation in the descending aorta [31, 32]. The wall shear stress is defined as the norm of the shear stress at the wall:

$$WSS = \|\vec{t_w}\| = \|\vec{t} - (\vec{t} \cdot \vec{n}) \cdot \vec{n})\|, \quad \text{with} \quad \vec{t} = \mu \left(\nabla \vec{u} + \nabla \vec{u}^T\right) \cdot \vec{n}. \tag{7}$$

For the numerical simulation, we apply simple boundary conditions: a parabolic velocity profile at the inlet (heart) and zero natural pressure boundary conditions at the outlets (innominate artery, left common carotid artery, left subclavian artery and descending aorta) and a zero velocity (no-slip) on the vessel walls. We consider a stationary flow at Reynolds $Re = 450$ and different meshes: isotropic volume meshes of respectively $28K$, $160K$ and $466K$ tetrahedra and an adapted anisotropic mesh that has approximately $20K$. We fist compute an isotropic surface mesh with our remeshing algorithm and then produce two different types of volume meshes: (i) isotropic volume meshes of different prescribed mesh sizes, (ii) adapted anisotropic volume meshes and (ii) a boundary layer mesh obtained by extrusion of the surface mesh over a number of layers (5 layers in the boundary $\delta = 1/\sqrt{Re}$). Adaptive refinement in the boundary with either anisotropic metric fields or boundary layers is indeed attractive [34, 35, 36] to increase the solution accuracy in the region of interest (at the wall) and

§`http://www-c.inria.fr/Eric.Saltel/saltel.php` this way decrease the load on the solver by reducing the number of finite elements used. With the presented approach of harmonic map, we do have a parametric description of the initial triangulation that enables us to use anisotropic mesh adaptation libraries such as our open source MadLib library [33]. This library aims at modifying the initial mesh to make it comply with criterions on edge lengths and element shapes by applying a set of standard mesh modifications (edge splits, edge collapses and edge swaps, ...). An anisotropic field based on the distance to the wall and the curvature can then be defined in order to generate boundary layer meshes. In the example presented in Fig.7c), we prescribe a small size with a linear growth in the normal direction to the wall, and three times a larger size is prescribed in the tangent directions. The final mesh metric field is built from those resulting sizes and directions. It should be noted that a volume mesh was also produced from the STL triangulation but this volume mesh was of too low quality to obtain a convergence of the numerical simulation ($\gamma_{min} = 1.5e^{-5}$ and $\bar{\gamma} = 0.45$).

Figure 7 shows the initial STL triangulation, a remeshed isotropic surface mesh, and a mesh cut of the volume anisotropic mesh. As can be seen, initial STL triangulation is faceted and the horizontal structure of the CT slices are visible.

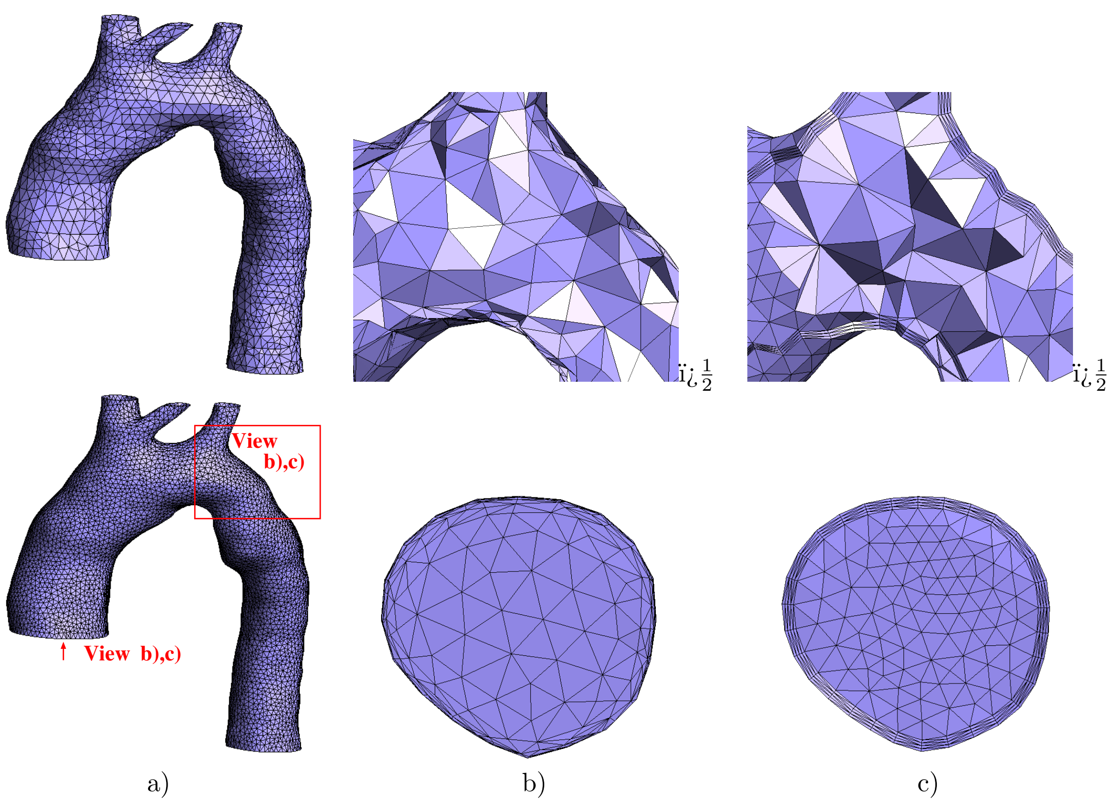

Figure 7. Aortic arch meshes: a) Initial STL triangulation (top) and remeshed surface (isotropic mesh size), b) Anisotropic volume mesh cut created from the remeshed surface with MAdLib, c) Boundary layer volume mesh.

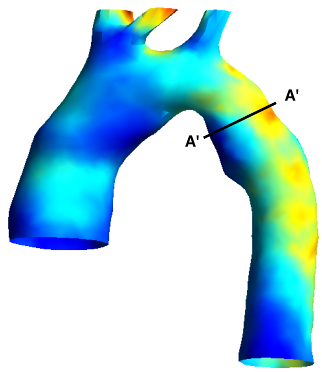

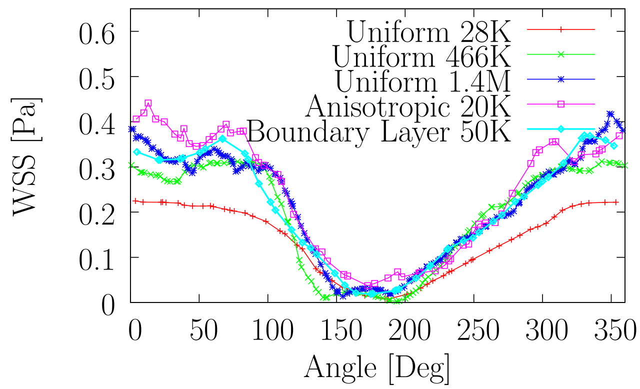

Figure 8. Blood flow simulation in an aortic arch. The left figure shows the WSS distribution and the right figure the WSS along the circumference at section $A - A'$ for different meshes for a constant inlet flow rate. The zero angle corresponds to the location A'.

Figure 8 shows the WSS values computed for different meshes at section $A-A'$. We selected section $A - A'$ since this section intersects the regions of low and high WSS. For this section, the WSS values vary in the azimuthal direction, the zero angle corresponding to the location A'. As can be seen in Fig.8, the high quality isotropic volume meshes converge well towards an azimuthal WSS distribution. The WSS for the anisotropic mesh exhibits more numerical noise that is due to the velocity gradient computations involved in (7) that are less accurate for highly anisotropic meshes [34, 35, 36]. Meanwhile, the mean values (max and min WSS) converge towards the one obtained with the finest isotropic mesh within a smaller computational time (mesh of only $20K$). The boundary layer volume mesh provides less oscillatory results and show also convergence towards the finest isotropic mesh for a reduced number of elements ($50k$ versus $1.4M$ tetrahedra).

The last biomedical computation is the stress computation on a hemipelvis. The initial triangulation (STL file) of the pelvic bone is obtained from a segmentation procedure of a sawbone model that was scanned (CT scan with 1.25 mm thickness). Several isotropic surface meshes are obtained with our automatic remeshing algorithm for different mesh refinements. We analyze the influence of the mesh quality on the accuracy of the solution : 5 meshes obtained with the uniform remeshing algorithm having respectively 420k, 270k, 70k, 20k and 5k triangles, 2 meshes that are adapted to the curvature with 54k and 8k triangles and 3 STL triangulations of 10k, 5k and 2k triangles (see Fig. 9). The 3 different STL files are obtained with the meshLab software by refining the triangles or collapsing the edges of the initial STL file of 5k triangles. As expected, the mean quality is $\bar{\kappa} = 0.94$ for the remeshed pelvis while $\bar{\kappa} = 0.66$ for STL triangulations. The curvature adapted meshes are computed by defining the mesh size δ as follows:

$$\delta = \frac{2\pi R}{N_p}, \quad \text{with } R = \frac{1}{\kappa} \tag{8}$$

where κ is the curvature that is computed from the initial nodes of the STl triangulation with the algebraic point set surface (APSS) method that is based on the local fitting of algebraic spheres [?] and N_p is the number of points chosen for the radius of curvature ($N_p = 15$).

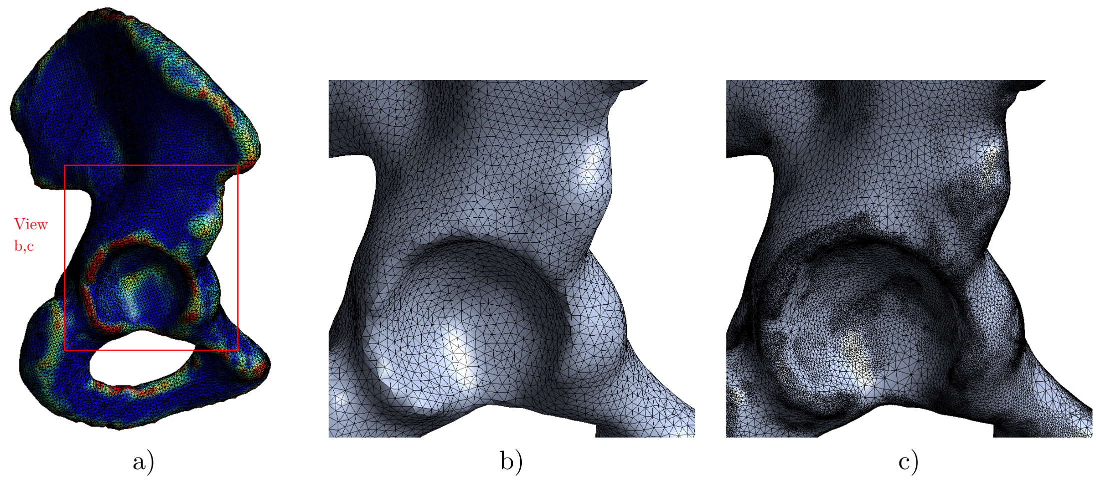

Figure 9. Different meshes used for the mesh convergence analysis. a) Triangulation on which a curvature κ is computed, b) isotropic remeshed pelvis ($\delta = 0.1$) and c) Curvature-dependent remeshed pelvis (δ given by Eq.(8)).

Figure 10 shows the boundary conditions used for the finite element computation. The finite element model is constrained at the sacro-iliac joint and a symmetry boundary condition is applied on the pubic-symphysis. The pelvis is subjected to a 3D load case representative of a single leg stance. Taking a body weight equal to 1000N, the resulting surface traction force acting on the acetabulum surface is $0.7\,MPa$. As different meshes are used, the elements forming the boundaries are selected inside a sphere (for the acetabulum and the sacrum) and on one side of a plane (for the pubis) intersecting the pelvis. These fixed boundary conditions are more representative of *in vitro* experimentation than *in vivo* environment but are realistic enough for this analysis [37].

In order to put to the fore the effect of the surface mesh on the behavior of the numerical solution, we analyze the stresses in the cortical bone by using shell elements on the surface of the pelvis. This is well adapted for this analysis because the pelvis has a cortical shell that undergoes most of the stresses. We model this cortical surface layer with a homogeneous shell section of uniform thickness $2mm$, an isotropic Young modulus $E = 18000 N/mm^2$ and a poisson ratio of $\nu = 0.3$ [38, 39].

The simulations are computed wih the finite element solver Abaqus with linear finite elements. Figure 11 shows the distribution of the Von-Mises stresses developed in the cortical bone with the finest isotropic mesh. The stresses are concentrated around the cotyle and toward the fixed boundary condition at the sacro-iliac joint. The maximum stresses are obtained around the cotyle for the fine meshes while the STL meshes produce higher stresses located above the illium. These are local stress concentrations that appear in small elements, where no significant stress should be present.

To determine the influence of the mesh quality on grid convergence, we consider different isotropic surface meshes and STL meshes and evaluate an absolute error measure of the

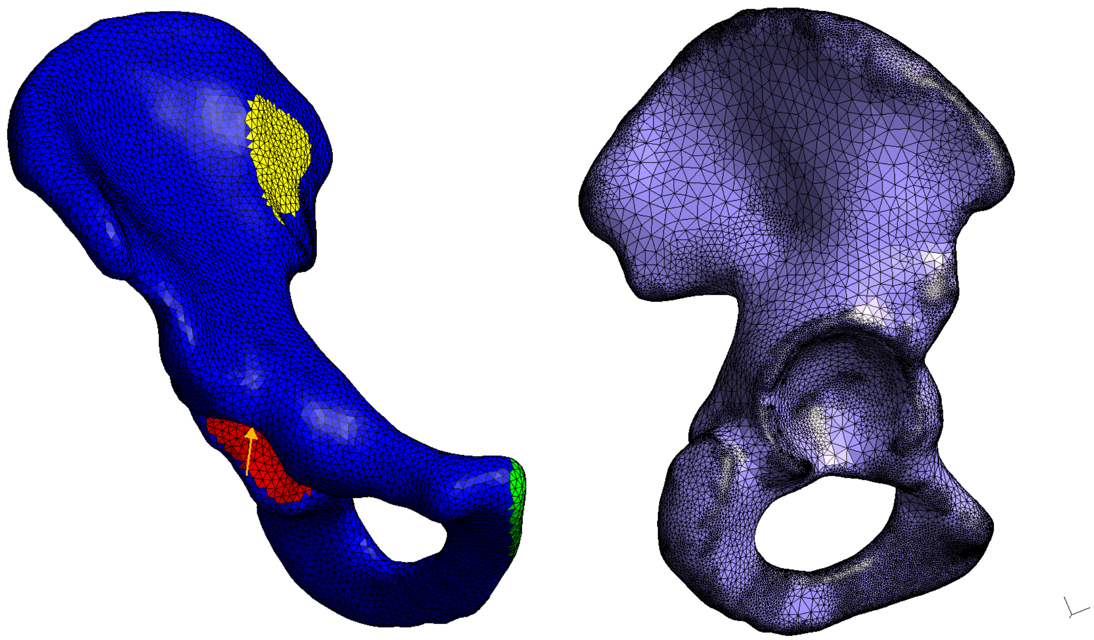

Figure 10. Finite element computations in the cortical shell. The left figure shows the boundary conditions. The right figure shows a non-uniform mesh that is refined in the areas of high curvatures.

displacement field between each of those meshes and the finest isotropic mesh computed with linear shell elements (420k elements). The total error ϵ_{total} for a mesh is given by taking the root mean square of the relative error ϵ_i for each vertex i of the reference mesh :

$$\epsilon_{total} = \frac{\sum_{i=0}^{N} \epsilon_i}{N}, \epsilon_i = \sqrt{\epsilon_{i1}^2 + \epsilon_{i2}^2 + \epsilon_{i3}^2}, \quad \text{where } \epsilon_{ij} = |u_{ij} - \bar{u}_{ij}|, \tag{9}$$

where N is the number of nodes of the reference mesh, u_{ij} is the jth component of the displacement for the ith reference mesh vertex and $\bar{u}_{ij}$ is the interpolation of the jth component of the displacement computed in the considered mesh at the location of the ith vertex. As 3D surface meshes do not coincide, the interpolation is computed at the projection on the closest surface element in this element.

Figure 11 shows the grid convergence for the different meshes, where we can clearly see the influence of the mesh quality on the convergence. The theoretical convergence for linear shell elements is of order $\mathcal{O}(h^2)$ and is recovered with our high quality meshes while the STL triangulations present a much lower convergence $\mathcal{O}(h^{0.2})$ as well as a higher error for the same number of nodes.

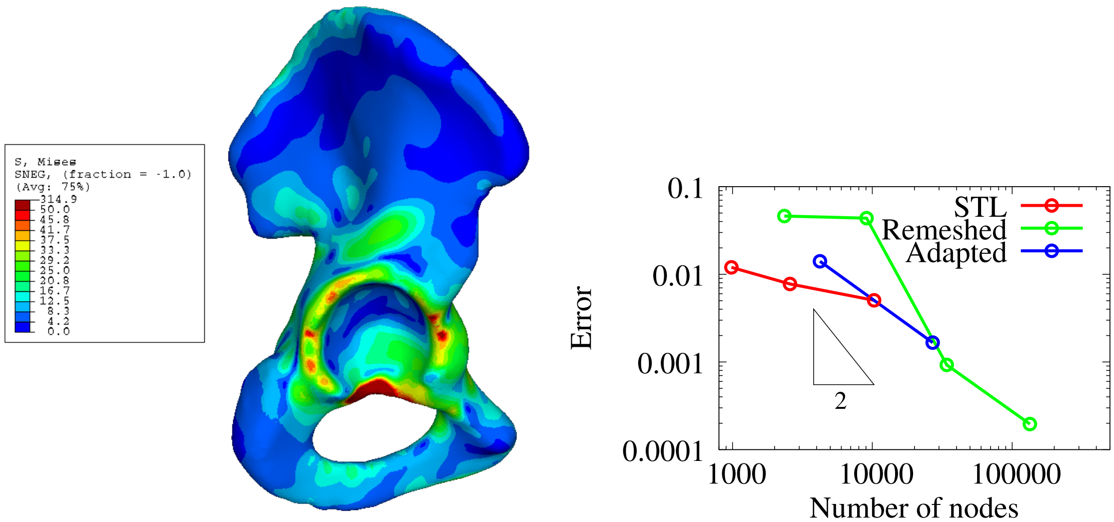

Figure 11. Von mises stress distribution in the cortical shell computed with the finest isotropic surface mesh (Left) and influence of the mesh quality on the numerical solution (Right).

5. CONCLUSION

In this work, we have presented a fully automatic approach to recover a high quality surface mesh from low-quality oversampled inputs (STL files) obtained via 3D acquisition systems. The approach is original as it combines an efficient and robust parametrization technique based on harmonic maps [1] with a multi-level edge partitioning algorithm that partitions the mesh in a small number of partitions. With the present approach, we are able to remesh any surface with any topological genus and with large geometrical aspect ratio such as arteries. We showed that the remeshing procedure is highly efficient and produces high-quality meshes that are suitable for finite element biomedical simulations. We have presented several biomedical computations that quantify the influence of the mesh quality on the convergence behavior.

ACKNOWLEDGEMENTS

The authors gratefully acknowledge the Belgian National Fund for Scientific Research (FNRS) and the Walloon Region (EFCONIVO Project) for their financial support.

REFERENCES

1. Remacle JF, Geuzaine C, Compère G, Marchandise E. High quality surface remeshing using harmonic maps. *International Journal for Numerical Methods in Engineering* accepted 2009; .
2. Geuzaine C, Remacle JF. Gmsh: a three-dimensional finite element mesh generator with built-in pre- and post-processing facilities. *International Journal for Numerical Methods in Engineering* 2009; **79**(11):1309–1331.

3. Gross M. Computer graphics in medicine: from visualization to surgery simulation. *ACM SIGGRAPH Computer Graphics* 1998; **32**(1):53–56.
4. Schoberl J. Netgen, an advancing front 2d/3d-mesh generator based on abstract rules. *Comput. Visual. Sci.* 1997; **1**:41–52.
5. Si H. Tetgen a quality tetrahedral mesh generator and three-dimensional delaunay triangulator 2004.
6. Szczerba D, McGregor R, Szekely G. High quality surface mesh generation for multi-physics bio-medical simulations. *Computational Science – ICCS 2007*, vol. 4487. Springer Berlin, 2007; 906–913.
7. Batdorf M, Freitag L, Ollivier-Gooch C. A computational study of the effect of unstructured mesh quality on solution efficiency. *Proc. 13th AIAA Computational Fluid Dynamics Conf.*, 1997.
8. Babuska I, Aziz A. On the angle condition in the finite element method. *SIAM Journal on Numerical Analysis* 1976; **13**:214–226.
9. Fried I. Condition of finite element matrices generated from nonuniform meshes. *AIAA Journal* 1972; **10**(219-221).
10. Ito Y, Nakahashi K. Direct surface triangulation using stereolithography data. *AIAA Journal* 2002; **40**(3):490–496.
11. Bechet E, Cuilliere JC, Trochu F. Generation of a finite element mesh from stereolithography (stl) files. *Computer-Aided Design* 2002; **34**(1):1–17.
12. Wang D, Hassan O, Morgan K, Weatheril N. Enhanced remeshing from stl files with applications to surface grid generation. *Commun. Numer. Meth. Engng* 2007; **23**:227–239.
13. Borouchaki H, Laug P, George P. Parametric surface meshing using a combined advancing-front generalized delaunay approach. *International Journal for Numerical Methods in Engineering* 2000; **49**:223–259.
14. Zheng Y, Weatherill N, Hassan O. Topology abstraction of surface models for three-dimensional grid generation. *Engrg. Comput.* 2001; **17**(28-38).
15. Marcum DL. Efficient generation of high-quality unstructured surface and volume grids. *Engrg. Comput.* 2001; **17**:211–233.
16. Tristano J, Owen S, Canann S. Advancing front surface mesh generation in parametric space using riemannian surface definition. *Proceedings of 7th International Meshing Roundtable*. Sandia National Laboratory, 1998; 429–455.
17. Laug P, Boruchaki H. Interpolating and meshing 3d surface grids. *International Journal for Numerical Methods in Engineering* 2003; **58**:209–225.
18. Levy B, Petitjean S, Ray N, Maillot J. Least squares conformal maps for automatic texture atlas generation. *Computer Graphics (Proceedings of SIGGRAPH 02)*, 2002; 362 – 371.
19. Floater MS, Hormann K. Surface parameterization: a tutorial and survey. *Advances in Multiresolution for Geometric Modelling* 2005; .
20. Sheffer A, Praun E, Rose K. Mesh parameterization methods and their applications. *Found. Trends. Comput. Graph. Vis.* 2006; **2**(2):105–171.
21. Marcum DL, Gaither A. Unstructured surface grid generation using global mapping and physical space approximation. *Proceedings, 8th International Meshing Roundtable*, 1999; 397–406.
22. Eck M, DeRose T, Duchamp T, Hoppe H, Lounsbery M, Stuetzle W. Multiresolution analysis of arbitrary meshes. *SIGGRAPH '95: Proceedings of the 22nd annual conference on Computer graphics and interactive techniques*, 1995; 173–182.
23. Shinagawa Y, Kunii T, Kergosien YL. Surface coding based on morse theory. *IEEE Computer Graphics and Applications* 1991; **11**(5):66–78.
24. Hendrickson B, Leland R. A multilevel algorithm for partitioning graphs. *In Proc. Supercomputing*, 1995.
25. Karypis G, Kumar V. A fast and high quality multilevel scheme for partitioning irregular graphs. *International Conference on Parallel Processing*, 1995; 113–122.
26. Chang CT, Gorissen B, Melchior S. Fast computation of the minimal oriented bounding box on the rotation group so(3). *ACM Transactions on Graphics* 2009, to appear; .
27. Durand N, Alliot JM. A combined nelder-mead simplex and genetic algorithm. *GECCO'99: Proc. Genetic and Evol. Comp. Conf*, 1999; 1–7.
28. George PL, Frey P. *Mesh Generation*. Hermes, 2000.
29. Marchandise E, Remacle JF. A stabilized finite element method using a discontinuous level set approach for solving two phase incompressible flows. *Journal of Computational Physics* 2006; **219**:780–800, doi: DOI10.1016/j.jcp.2006.04.015.
30. Ethier CR, Prakash S, Steinman DA, Leask RL, Couch GG, Ojha M. Steady flow separation patterns in a 45 degree junction. *Journal of Fluid Mechanics* 2000; **41**:1–38.
31. O'brien KD, Chait A. The biology of the artery wall in atherogenesis. *The Medical clinics of North America* 1994; **78**(1):41–67.
32. Shaaban AM, Duerinckx A. Wall shear stress and early atherosclerosis. *American Journal of Roentgenology* 2000; **174**:1657–1665.
33. Compère G, Remacle JF. Website of madlib: Mesh adaptation library 2008. http://www.madlib.be.

34. Sahni O, Mueller J, Jansen K, Shephard M, Taylor C. Efficient anisotropic adaptive discretization of cardiovascular system. *Comp. Meth. Appl. Mech. Eng.* 2006; **195**:5634–5655.
35. Sahni O, Jansen K, Shephard M. Automated adaptive cardiovascular flow simulations. *Engineering with Computers* 2009; **25**(1):25–36.
36. Botti L, Piccinelli M, Ene-Iordache B, Remuzzi A, Antiga L. An adaptive mesh refinement solver for large-scale simulation of biological flows. *Communications in Numerical Methods in Engineering* 2009; .
37. Phillips A, Pankaj P, Howie C, Usmani A, Simpson A. Finite element modelling of the pelvis: Inclusion of muscular and ligamentous boundary conditions. *Medical engineering and physics* 2007; **29**(7):739–748.
38. Dalstra M, Huiskes R. Load transfer across the pelvic bone. *Journal of Biomechanics* 1995; **28**:715–724.
39. Anderson A, Peters C, Tuttle B, Weiss J. Subject-specific finite element model of the pelvis: development, validation and sensitivity studies. *J Biomech Eng* 2005; **127**(3):364–373.